JOURNAL OF MATERIALS SCIENCE **37** (2002) 3999–4011

Identification of the viscoplastic behavior of a polycarbonate based on experiments and numerical modeling of the nano-indentation test

J. L. BUCAILLE, E. FELDER*
Centre de Mise en Forme des Matériaux, Ecole des Mines de Paris, 06904 Sophia Antipolis, France
E-mail: eric.felder@cemef.cma.fr

G. HOCHSTETTER
Essilor International, 94106 Saint Maur des Fossés, France

Indentation testing is a convenient means to study mechanical properties of thin coatings. We suggest a new method to identify the viscoplastic behavior of a polymer by using the force-penetration curves during nano-indentation testing performed with two indenter shapes. During loading, the load applied by the indenter and the penetration depth have been measured. These force-penetration curves have been compared to the load computed by using the finite element method with a two dimensional software. The viscoplastic behavior of the polymer is modeled with the G'sell-Jonas law. The main particularity of this law is the modeling of the large strain-hardening at large strains. The unknown parameters of this law have been obtained by fitting computed and experimental force-penetration curves. We have identified each parameter independently of the others by taking into account the indenter tip defect. The nano-indentation tests have been performed with three strain rates and with two indenter shapes: a Berkovich indenter and a cone with a semi angle of $\theta = 30^\circ$ and a tip radius. In this paper, the polymer is a polycarbonate. Several authors have made rheological tests on this polymer. The true strain-true stress curve obtained with our method is in good agreement with the compression curve.

1. Introduction

Indentation is a method to identify the mechanical properties of materials near their surfaces: normal hardness and yield stress as a function of strain. This test can be performed on thin coatings with a thickness below 3 μm, at this scale compression or tension tests can not be performed. It is important to be able to measure yield stress and strain during such a test.

The mean contact pressure (or normal hardness), H_n, can be related to the flow stress, σ_0, of the material, for a representative strain, by the following expression [1]:

$$\frac{H_n}{\sigma_0} = C, \tag{1}$$

where the normal hardness is equal to the ratio of the normal load applied on the indenter, F, to the projected area. For an axisymmetrical indenter (Fig. 1):

$$H_n = \frac{F}{\pi R_c^2}, \tag{2}$$

where R_c is the contact radius under load. The yield stress of work-hardened metals is quite constant, but for materials which work-harden, the yield stress increases as the strain increases. For such materials, the yield stress is always related to a value of the strain. The constant C is between 2.8 and 3.3 for indentation with blunt indenters on metals [1]. For a rigid-plastic material indented by cones, the constant C also varies as the angle of the indenter varies [2, 3], $1.8 < C < 2.5$. Johnson [4] has suggested a general value to $\frac{H_n}{\sigma_0}$ which depends on the rheological factor, X:

$$X = \frac{E}{\sigma_0} \tan\beta, \tag{3}$$

where E is the Young's modulus and β is the angle of inclination of the indentation at its edge. This ratio can be interpreted as the ratio of the strain imposed by the indenter to the maximum strain which can be accommodated by the material before yielding. As this factor is close to 10, the deformation imposed by the indenter is elastoplastic with a large elastic part of the whole deformation. As this factor increases and becomes close to 100, the deformation becomes mainly plastic. The ratio $\frac{H_n}{\sigma_0}$ increases from 1 to 3 as $\frac{E}{\sigma_0}\tan\beta$ increases. In

---

*Author to whom all correspondence should be addressed.

0022–2461 © *2002 Kluwer Academic Publishers*

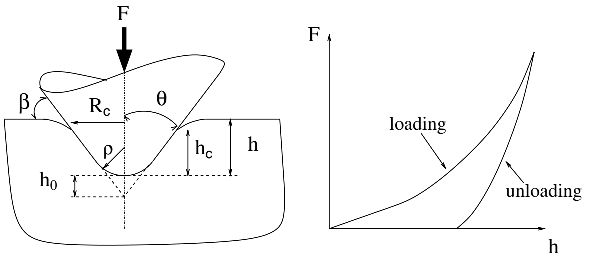

Figure 1 Geometrical parameters under load and typical force-penetration curve, with a cone with a tip defect. These are the usual contact geometry and force-penetration curve for a polymer.

order to compute hardness, the contact radius has to be measured under load. Because of the very small penetration depths during nano-indentation, the measure of the contact radius, used to compute normal hardness, is particularly difficult. The elastic recovery for polymers is very large, the radius measured after unloading is not equal to the contact radius under load. Methods have been then developed to compute hardness with the force penetration curve obtained during unloading in indentation or nano-indentation [5]. The relation between hardness and yield stress depends on several parameters, but it is quite well established.

For conical indenters, the strain field is independent of the penetration depth of the indenter. In indentation with cones on metals, Johnson [4] has suggested a definition of the representative strain:

$$\varepsilon_r = 0.2 \cot\theta, \tag{4}$$

where θ is the semi angle of the indenter (Fig. 1). Such a formula has not been established for elastoplastic materials, for which the proportionality constant between the representative strain and $\tan\beta$ may be different [6].

So, Equations 1 and 4 allow to compute and to plot strain-stress curves in indentation for metals, but, it is not the case for materials with a large elastic part, such as polymers. These are the main reasons why, in the last few years, authors have obtained the stress-strain relationship of materials by matching loading and unloading curves calculated using the finite element method (FEM) with those measured experimentally. Bhattacharya and Nix [7] have considered a conical indenter indenting elastic perfectly-plastic materials, which have been modeled with three parameters: the Young's modulus, the Poisson's ratio and the yield stress. For elastoplastic materials which work-harden, Cheng and Cheng [8] have shown that several stress-strain curves can be obtained for a given loading and unloading curve. So, they have suggested to use several indenters to obtain the stress-strain relationship. Venkatesh *et al.* [9] and Tardieu [10] have presented reverse analysis based on indentation experiments with a Vickers or a Berkovich pyramid on elastoplastic materials. They have considered that their method allows to obtain a unique stress-strain relationship. Simulations have been performed with a frictionless contact, because with large angle indenters, friction has no noticeable influence on the force-penetration curve. Furthermore, during indentation experiments, the interface between the specimen and the indenter has been lubricated.

In this paper, the viscoplastic behavior of a polymer has been identified with two indenters and with three strain rates by using the loading curves. The elastic behavior is assumed to have been previously identified using compression tests and unloading curves in indentation. The indenter tip defect has been taken into account and two conditions of friction at the interface between the indenter and the mesh have been chosen. In order to verify if our method is efficient, stress-strain curves have been compared with compression and tension tests. This is the reason why we have chosen a polymer where tension and compression tests can be performed: polycarbonate. Such comparisons can not be performed on polymers used to make thin coatings.

2. Experimental and numerical method

2.1. Experiments on polycarbonate

Nano-indentation experiments have been performed with the Nanoindenter II®, commercialised by MTS. These experiments have been made at Essilor International. Two diamond indenters have been used:

- A cone of semi apical angle 30°; its tip has been modeled as a part of a 600 nm radius sphere, estimated with a scanning electron microscope.
- A Berkovich indenter, i.e., a three-faced pyramid with a sharply pointed tip [11].

The normal force, F, and the depth of indentation, h, have been measured during the indenter penetration (Fig. 1). During the test, the load applied to the indenter has been controlled. The maximum normal force imposed to the indenter during experiments is about 2 mN. The maximum depths are about 2 μm for the conical indenter and 0.7 μm for the Berkovich pyramid. The zero-point, defined as $F = 0$ and $h = 0$, has been determined by a change in the force signal as the indenter approaches the test surface. For polymers, there are uncertainties in determining the point of tip-sample contact, so that $F = 0$ does not correspond to $h = 0$. The value of the error was estimated of about 10 nm. For elastoplastic materials such as polymers, the elastic part of the whole deformation is large. The elastic behavior is very intricate and depends, in particular, on strain and strain rate [12, 13]. The finite element code chosen to simulate the polycarbonate indentation cannot model such a complex behavior. Consequently the focus is only on the force-penetration curves during loading.

In order to have a constant mean strain rate during the indentation by a perfect cone or pyramid, the ratio $\frac{\dot{F}}{F} = c$, must be constant [14], c is the loading rate, $\dot{F}$ is the differentiation of the load with respect to the time. So, for constant loading rate, constant mean strain rate is induced by real conical and pyramidal indenters for very large penetrations compared to the tip defect, h_0. But at the beginning of the penetration, and for the cone of semi apical angle 30° and 600 nm tip radius, the mean strain rate is not constant, with such a kinematic. We chose three load speeds: $c = 0.1\ \mathrm{s}^{-1}$, $c = 0.01\ \mathrm{s}^{-1}$, $c = 0.001\ \mathrm{s}^{-1}$, for each indenter. For $F = 0$, the ratio $\frac{\dot{F}}{F}$ is infinite; so at the beginning, the normal force is constant and equal to 20 μN.

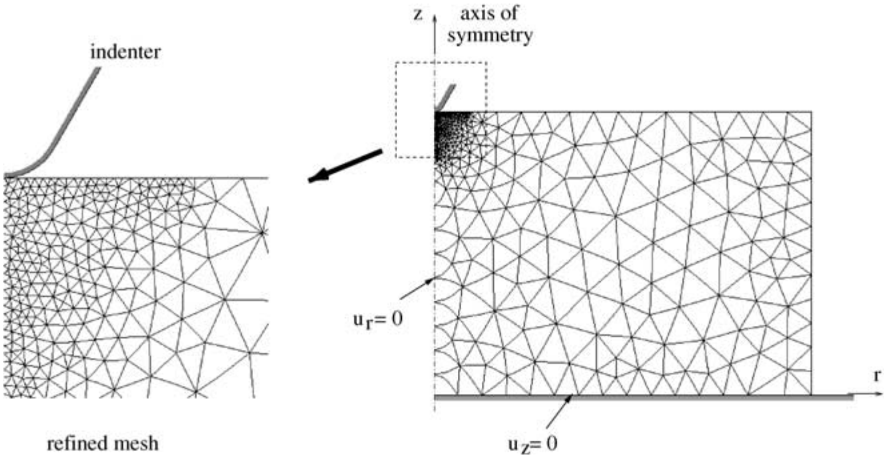

Figure 2 Finite element mesh for the indentation simulation.

2.2. Two dimensional numerical method

The software used is a two dimensional axisymmetric finite element code: Forge2®. The main feature of this code is the automatic remeshing procedure. The cone with a tip defect is modeled with exactly the same geometry: semi apical angle 30° and $\rho = 600$ nm. The Berkovich pyramid is approximated by an axisymmetric cone of equal volume for the same penetration depth. The semi apical angle of this equivalent cone is equal to 70.3°. First, we shall consider that this indenter has no tip defect. The indenters are considered to be perfectly rigid. A typical mesh, composed of six-noded triangles, is displayed in Fig. 2. To have a good representation of the contact geometry, elements are small near the indenter. The typical length for an element is about 0.10 μm, meshes are larger far from the indenter: 3 μm. During preliminary simulations, the size of the mesh was increased to show that this change has no effect on the force-penetration curves. When elements are too much degenerated, the code remeshes automatically. For the maximal depths of the experiments, simulations of indentation need at least seven remeshing procedures for the blunt cone and only three for the indenter of semi apical angle 30°.

Simulations with a control of the load applied on the indenter requires far more CPU time than those with a control of the indenter speed. So, during the simulation the indenter speed is controled. A similar kinematic as the one used during experiments has to be imposed. For a pyramid or a cone, and for large penetration depths compared to the tip defect ($h \gg h_0$), the force is proportional to the square of the penetration [8]:

$$F = Dh^2 \tag{5}$$

$$\Rightarrow \frac{\Delta F}{\Delta t} = \dot{F} = 2D\dot{h}h \tag{6}$$

$$\frac{\dot{F}}{F} = c = 2\frac{\dot{h}}{h} \tag{7}$$

During indentation experiments with the Berkovich indenter, ratios $\frac{\dot{F}}{F}$ and $\frac{\dot{h}}{h}$ have been measured (Table I). Relationship 7 is valid, as the difference is less than 10 per cent. So, in simulation, the indenter speed is, at first, constant, and for $h > 50$ nm the ratio $\frac{\dot{h}}{h}$ is constant and equal to the values reported in Table I. For the conical indenter, the kinematic is not exactly the same during the beginning of the penetration. However, it will be shown later that force-penetration curves of this indenter are most interesting for large penetrations.

TABLE I Comparison between the ratios $\frac{\dot{F}}{F}$ and $\frac{\dot{h}}{h}$ for the Berkovich indenter

$\frac{\dot{F}}{F}$ (s^{-1})	0.1	0.01	0.001
$\frac{\dot{h}}{h}$ (s^{-1})	0.0493	0.00536	0.000548

3. The modeling of the polymer behavior

3.1. The viscoplastic model

With its automatic remeshing procedure, the finite element software used (Forge2®) allows to simulate the large penetrations and strains imposed during indentation test. This software is mostly used to simulate metals forging, the rheological laws to model the behavior of solid polymers are quite poor. We discuss below about these insufficiencies:

- The elastic behavior of polymers depends in particular on strain and strain rate [13]. However, the elastic behavior is modeled by a linear law. The parameters defining the material elastic behavior are the Young's modulus, E, and the Poisson's ratio, ν. These parameters are constant.
- For glassy polymers, the true stress rises to a maximum value, this is the end of the purely viscoelastic behavior. As the strain increases, the stress drops. This behavior is also observed in shear and compression for true stress-true strain curves (Fig. 3). It is impossible to model this strain softening with the finite element software we use.
- The plastic part of the deformation is based on the von Mises criterion, which supposes that the material is isotropic. This criterion does not take into account the hydrostatic pressure, nor the anisotropy due to material orientation. The influence of the hydrostatic pressure on polymers is reflected by the difference between the tension and compression stress-strain curves in Fig. 3 at small strains.

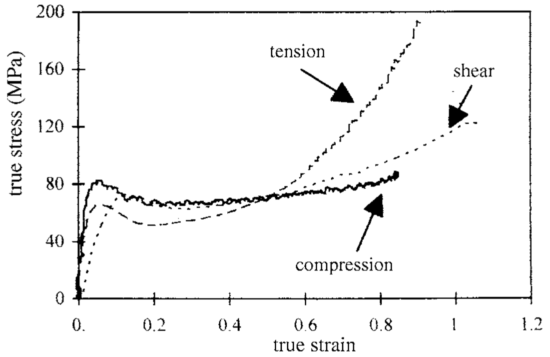

Figure 3 True stress-true strain curves for polycarbonate [16], true strain rate $= 10^{-4}$ s^{-1}, $T = 23°$C.

> Many authors have also shown the influence of the hydrostatic pressure on polymers [12, 13]. For a constant strain, stress for a polycarbonate increases to 35% and 65% as hydrostatic pressure increases respectively to 100 MPa and 200 MPa [15].

Despite these approximations, the best law available in the software to model polymers behavior, is the law presented below.

After studying the behavior of several polymers in tension, G'sell and Jonas [17] present the following law:

$$\sigma_0(\bar{\varepsilon}, \dot{\bar{\varepsilon}}, T) = K e^{\frac{a}{T}}(1 - e^{-w\bar{\varepsilon}})e^{h_g\bar{\varepsilon}^2}\dot{\bar{\varepsilon}}^m \tag{8}$$

This law links the true stress, σ_0 to the true strain, $\bar{\varepsilon}$. It assumes a temperature dependence with the exponential term $e^{\frac{a}{T}}$, and a strain rate dependence with a power law $\dot{\bar{\varepsilon}}^m$. The parameters a and m are constant, a is a thermal coefficient and m is the sensitivity to the strain rate. So true stress-true strain curves for a polycarbonate are split in four parts (Fig. 3):

- A purely viscoelastic deformation at low strain, it is almost linear and the slope is large. This part is modeled by the term $(1 - e^{-w\bar{\varepsilon}})$ of Equation 8.
- The stress reaches a local maximum value and after the stress drops. This strain softening exists for glassy polymers like polycarbonate. It is not taken into account in the formulation representing the material viscoplastic behavior (Equation 8).
- As strain increases, the flow stress slowly increases. This part is called the viscoplastic level. The consistency K, multiplied by the $e^{\frac{a}{T}}$ and $\dot{\bar{\varepsilon}}^m$ terms, is a medium value of this viscoplastic level.
- At larger strains the flow strain strongly increases. This large strain hardening is related, in tension, to the macromolecules orientation in the drawing direction. It is higher and it begins earlier in tension than in shear and compression. The $e^{h_g\bar{\varepsilon}^2}$ term models this strain hardening, h_g is called the hardening modulus.

3.2. Discussion about strain hardening at large strains

The large strain hardening for polymers during tension is due to the macromolecules orientation in the drawing direction. Compression tests on polycarbonate [16, 18] (Fig. 3) have shown that this strain hardening also exists in compression: true stress increases to 80 MPa and 280 MPa as true strain increases to 0.6 and 1.2 respectively. Hardening in tension is a result of an uni-axial orientation process, whereas in compression planar orientation is achieved [18]. X-ray observations made par Bisilliat [16] confirm this behavior. The strain hardening in shear stress is lower than in tension, but larger than in compression. In compression or shear, macromolecules are less oriented than in tension, so strain hardening is lower and begins later (Fig. 3). This is the reason why the G'sell-Jonas law is also used to model compression and shear behavior.

The indentation test is a multi-axial test. The G'sell-Jonas law has been formulated first for uni-axial tests such as tension test. The use of this law to simulate the indentation test assumes that this strain hardening also exists for polymers put through multi-axial tests. Bisilliat [16] made X-ray analysis for an impact test on a polycarbonate; this test is bi-axial. The polymer is bi-axially oriented and the intensity of the strain hardening is equal to the one observed in compression and shear. Even if the strain rates in an impact test are higher than in an indentation or in a tension test, the strains are in the same order of magnitude. And this is the most important reason, why we focus on the use of this law. Therefore, the high strain hardening observed in uni-axial tests was found to exist in multi-axial tests.

So, these facts suggest that the G'sell-Jonas law could describe, in first approximation, the polymer behavior during indentation or scratch, we shall discuss this point later (Section 5.1).

3.3. The elastic model

Although elastic behavior of a polymer is complex, the elasticity has been modeled with a linear law, the only model available in the finite element codes used. The parameters are Young's modulus, E, and Poisson's ratio, ν. These parameters have been deduced from compression tests at Essilor International: $E = 2.4$ GPa, $\nu = 0.35$. The Young's modulus value has been also confirmed with nano-indentation tests by using the force-penetration curves during unloading.

The G'sell-Jonas law describes the visco-elastic behavior for small strains with the $(1 - e^{-w\bar{\varepsilon}})$ term. In Forge®, the instantaneous deformation increment is separated in an elastic reversible part and a plastic irreversible part. The first part is computed with the elastic parameters (E and ν). When plastic deformation occurs, the second one is computed with the G'sell-Jonas law. This law models at the same time the behavior for small and large strains (Section 3.1), so for small strains the polymer behavior is modeled by both the elastic parameters (E and ν) and by the G'sell-Jonas law with the $(1 - e^{-w\bar{\varepsilon}})$ term. In order to have a behavior, for small strains, which is only modeled by the Young's modulus, the $(1 - e^{-w\bar{\varepsilon}})$ term must be equal to 1. This is the reason why we have chosen a very large value for w. For the next simulations, this parameter is equal to 5000.

3.4. Thermo-mechanical dependence; parameter *a*

The value of the thermo-mechanical dependence parameter a, obtained by Bisilliat [16] is 774 K^{-1} ($e^{\frac{a}{T}}$).

TABLE II Thermal effect on the consistency of a polycarbonate, $a = 774\ K^{-1}$

T (°C)	20	25	30	35	40
$e^{\frac{a}{T}}$	14	13.4	12.9	12.3	11.9

Simulations of indentation with thermo-mechanical dependence and without friction show at the most a 10°C increase in temperature. Consistency decreases by 8% (Table II). This heating, due to the dissipated energy resulting from the plastic deformation very, is localized and it has no significant effect on the force-penetration curves or on normal hardness. Thermo-dependence will be ignored during the simulations of indentation: the value of the parameter a is taken equal to zero.

3.5. Coulomb's friction coefficient μ

The friction between the material and the indenter is modeled with a Coulomb's law. The friction shear stress is equal to the normal pressure multiplied by the friction coefficient μ:

$$\tau = \mu p \tag{9}$$

This coefficient is constant at each contact point. Its value was estimated with scratch tests on polycarbonate performed at Essilor International, according to a procedure described in details in [19] and summarized here. During scratch test, normal force and tangential force applied to the indenter are measured. The ratio between the tangential force and the normal force is called the apparent coefficient of friction, μ_0. This coefficient is not the same as the local Coulomb's friction coefficient. By using analytical models, the apparent coefficient of friction has two components, a ploughing part μ_p, and an adhesive part μ_a [20]:

$$\mu_0 = \frac{F_t}{W} = \mu_p + \mu\mu_a \tag{10}$$

For a conical indenter with a large tip radius, analytical expressions of μ_p and μ_a have been obtained with the following hypothesis:

- the contact pressure is constant at the interface;
- the contact radius is constant at the front and on the side of the indenter;
- there is a complete elastic recovery at the rear face of the indenter;
- the shear stress is assumed to be parallel to the sliding direction.

The apparent coefficient of friction is measured during the scratch test, the ploughing and the adhesive parts are computed using the analytical expressions of μ_p and μ_a, the indenter geometry and the penetration of the indenter in the material. The Coulomb's friction coefficient is deduced with the Equation 10, its value was about 0.3. This coefficient was supposed to be constant with the strain rate and the strain. We have supposed that this coefficient was the same in indentation and scratch. In order to see the influence of this coefficient on the rheology, we have also identified the parameters for a friction coefficient, μ of 0.

4. Numerical results

We have to identify three parameters:

- m, sensitivity to the strain rate;
- K, consistency;
- h_g, hardening modulus.

The process that we will describe allows these parameters to be identified in three separated parts. We will compare force-penetration curves measured with the nano-indentation test, with those computed with the numerical modeling. For the identification of m, the consistency and the hardening modulus have been chosen close to the values obtained by Bisilliat [16] in compression and tension on a polycarbonate: $K = 88\ \text{MPa} \cdot \text{s}^{-m}$, $h_g = 0.9$.

4.1. Identification of the sensitivity to the strain rate, m

For a perfect pyramidal or conical indenter, the force during loading is proportional to the square of the penetration [8] (appendix, with $R^* = h^* = 0$). In this section, we assume that the Berkovich indenter has a perfect pointed tip. As we will see, we consider a difference between two values, so, this assumption is of no consequence. To identify the sensitivity to the strain rate, the apparent hardness is used:

$$H_{app} = \frac{F}{\pi R^2} \tag{11}$$

F is the normal force, and $R = h \tan\theta$, h is the penetration depth (Fig. 1). The apparent hardness is a different way to represent the force versus penetration. With the Berkovich indenter, the apparent hardness is relatively constant with the penetration (Fig. 4a). So, it is easier to compare the value of the apparent hardness than the evolution of the force during loading. For several simulations performed with various values of m, we have measured the difference of apparent hardness for two loading rates: $c = 0.1\ \text{s}^{-1}$ and $c = 0.001\ \text{s}^{-1}$: ΔH_{app}. Even if the Berkovich indenter is considered to have no tip defect, the error in the value of the apparent hardness is cancelled because we have computed the difference between two values of apparent hardness. The ratio $\frac{\Delta H_{app}}{\bar{H}_{app}}$ is computed, where $\bar{H}_{app}$ is the mean value of the apparent hardness for the two loading rates. This ratio is equal to zero for $m = 0$ and increases with m (Fig. 4b). The points are fitted by a linear regression. The sensitivity to the strain rate is deduced from this regression and from the experimental value of this ratio.

The sensitivity to the strain rate assuming either $\mu = 0$ or $\mu = 0.3$ are reported in Table III. The apparent sensitivity to the strain rate is a little larger for $\mu = 0.3$ than for $\mu = 0$. Values obtained by Bisilliat [16] are equal to 0.04 for compression and tension, and 0.02 for shear. The material in indentation seems to be

TABLE III Sensitivity to the strain rate for a polycarbonate, for two values of the Coulomb's friction coefficient

$\mu = 0$	$m = 0.046$
$\mu = 0.3$	$m = 0.053$

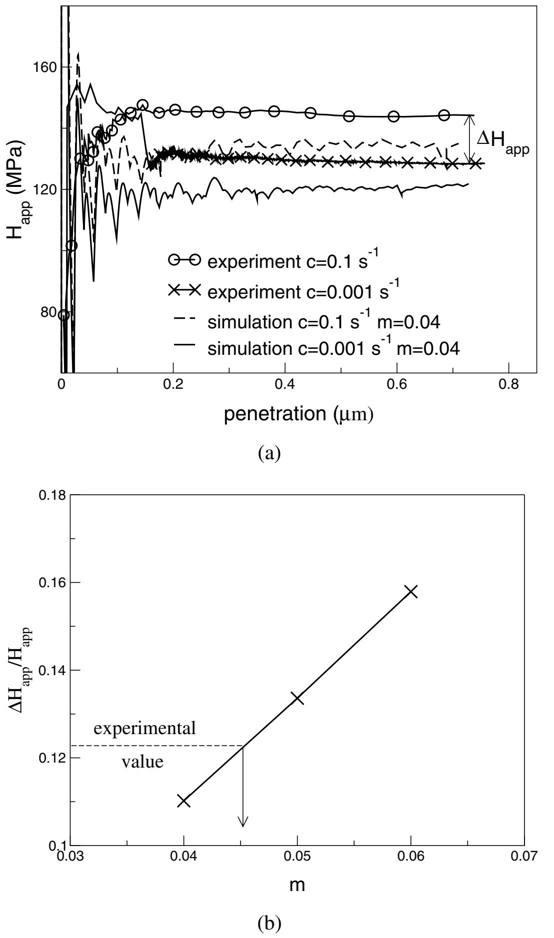

(a)

(b)

Figure 4 Apparent hardness with the Berkovich indenter for two loading rates ($c = 0.1\ \mathrm{s}^{-1}$ and $c = 0.001\ \mathrm{s}^{-1}$). The theoretical values are obtained with $\mu = 0$, $h_g = 0.9$, $K = 88\ \mathrm{MPa} \cdot \mathrm{s}^{-m}$. (a) Theoretical and experimental evolution versus the penetration. (b) Theoretical evolution of the relative increase in apparent hardness at high penetration, $\Delta H_{app}/\bar{H}_{app}$, versus the sensitivity to the strain rate m and experimental value.

more sensitive to the strain rate than in compression or tension.

The difference between force-penetration curves for several loading rates is now determined. On the other hand the values of the apparent hardness are higher for experiment than for simulation (Fig. 4a). The identification of the consistency in the next section will allow to fill this gap.

4.2. Identification of the consistency K

Locally, strains are not homogeneous in the volume (Fig. 5). Tabor [1] has suggested a representative value of the plastic strains; for conical indenters the representative strain is proportional to $\cot\theta$, Equation 4 [4]. This relationship gives an average of the plastic strains imposed by the indenter. An indenter of semi angle 30° produces a representative strain five times larger than for an indenter of semi angle 70.3°. In the simulations, the equivalent plastic strain, ε_{eq}, is computed for each element of the mesh:

$$\varepsilon_{eq} = \int_0^t \left[\frac{2}{3}\dot{\varepsilon} : \dot{\varepsilon}\right]^{1/2} \mathrm{d}t, \tag{12}$$

where $\dot{\varepsilon}$ is the plastic strain rate tensor. The simulations show that most of the material is strained to a level less than 0.4 for the 70.3° cone (Fig. 5). For the predicted plastic strains, stress is essentially constant, it is corresponding to the viscoplastic level (Fig. 3). This level is modeled by the consistency K which is identified with the Berkovich pyramid and its equivalent cone.

The other indenter has a large tip defect ($h_0 = 0.3\ \mu$m). For small penetration depths, we have verified that equivalent plastic strains are quite similar to those computed with the 70.3° indenter. As penetration increases, the equivalent plastic strains increase until a constant level is reached for large penetration depths. Equivalent plastic strains continue to increase even when the spherical part of the indenter is completely in the material. We suggest that the representative strain for such an indenter is proportional to the ratio $\frac{h_c}{R_c}$:

$$\varepsilon_r \sim \frac{h_c}{R_c} \tag{13}$$

where h_c is the contact penetration and R_c the contact radius (Fig. 1). For small penetrations, $\frac{h_c}{R_c}$ is equivalent to $\frac{R_c}{2\rho}$, this is the relationship given by Tabor [1] for spherical indenters. For large penetrations, $\frac{h_c}{R_c}$ is equivalent to $\cot\theta$.

For the 70.3° cone and the Berkovich indenter with a tip defect, the square root of the force is a linear function of the penetration depth (appendix):

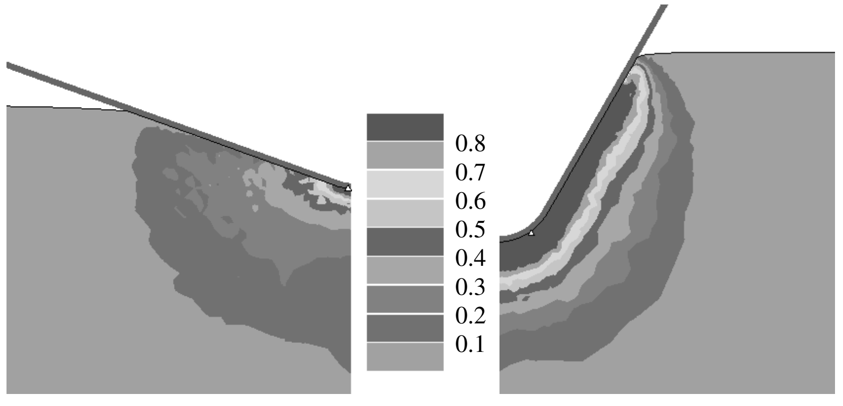

θ = 70.3°

maximum: 1

θ = 30° ρ = 600 nm

maximum: 1.8

Figure 5 Equivalent plastic strain computed with the finite element code®, in indentation for two indenters. $m = 0.046$, $K = 99$, $h_g = 0.8$, $\mu = 0$.

$$\sqrt{F} = Ah + B \tag{14}$$

Hence, we consider that the Berkovich indenter has a tip defect. The slope A is related to the semi angle of the indenter and the contact pressure, the parameter B is related to the semi angle of the indenter, the contact pressure and the indenter tip radius. For a given loading rate ($c = 0.1\ \text{s}^{-1}$), the experimental slope, A, is identified, for penetration depths higher than 400 nm. For several numerical simulations with different values of the consistency, A is computed (Fig. 6). These points are fitted using linear regression to estimate the consistency. There are dispersions due in particular to numerical uncertainty and the choice of the penetration depth from which the experimental slope is fitted. We estimate that the uncertainty is about ±4% for the identification of the consistency. The determination of the sensitivity to the strain rate has been previously performed by starting with the value $K = 88\ \text{MPa}\cdot\text{s}^{-m}$. As this determination is based on the relative increase of apparent hardness with two loading rates, $\Delta H_{app}/\bar{H}_{app}$, and that the final value of K is 12 percent higher, we assume that it is not necessary to estimate again the value of m.

Results are reported in Table IV. Consistency increases a little as friction coefficient increases. Although this increase is small (3%) and can be neglected in first approximation, it is rather surprising as we could expect that the indentation load increases with friction and so that the identified value of consistency decreases as the assumed value of friction coefficient increases. During indentation, the normal force per surface unit is the sum of two terms, a pressure component, p_y, and a shear component, τ_y (Fig. 7a):

$$f = p_y + \tau_y = p \sin\theta + \tau \cos\theta \tag{15}$$

For the indenter of semi apical angle 70.3°, the shear component is quite small (sin 70.3 = 0.94; 0.3 cos 70.3 = 0.10), and the contact pressure is the larger component. Medium values of the contact pressure, p_{medium}, and the shear stress, τ_{medium}, have been computed for $\frac{R}{R_c} \leq 0.9$ (Fig. 7). In fact, the contact pressure decreases when friction is taken into account (Fig. 7b, $p_{\text{medium}} = 193$ MPa, for $\mu = 0$, and $p_{\text{medium}} = 180$ MPa, for $\mu = 0.3$). The friction component does not fill this difference because the value of $\cos\theta$ is too small: $f_{\text{medium}} = 182$ MPa, for $\mu = 0$ and $f_{\text{medium}} = 179$ MPa, for $\mu = 0.3$. This is the reason why the apparent consistency for a rough contact is a little higher than for a frictionless contact. The opposite evolution, as we could expect, will be observed for the evolution of the hardening modulus (Section 4.4) as μ increases from 0 to 0.3.

The consistency K is identified before the hardening modulus, which is chosen arbitrarily. By increasing the parameter h_g from 1.3 to 7.5, we have verified that it had no significant effect on the force-penetration curves for the simulation with the 70.3° indenter. For a high value of the hardening modulus, the strain hardening is larger and begins earlier. But for the deformation levels imposed by the 70.3° cone, the flow stress is quite constant and it is not affected by the increase of h_g. The identification of the consistency is thus independent from the value of the hardening modulus.

TABLE IV Consistency K for two values of the Coulomb's friction coefficient. Identification of the tip radius of the 70.3° angle indenter

$\mu = 0$	$K = 99$	$\rho = 455$ nm
$\mu = 0.3$	$K = 102$	$\rho = 580$ nm

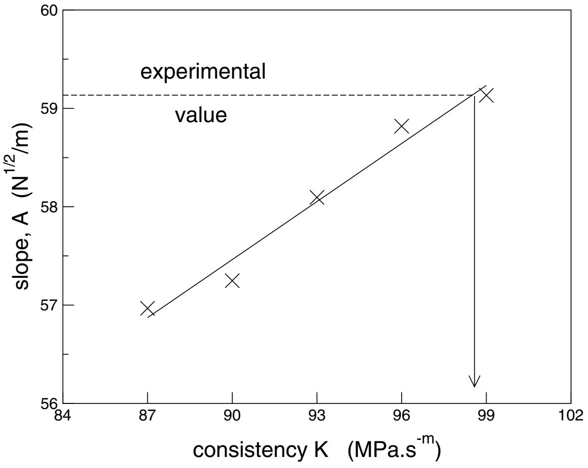

Figure 6 Slope A ($\sqrt{F} = Ah + B$) versus consistency. The experimental slope is 59.14, the consistency found is approximately equal to 99, for $\mu = 0$.

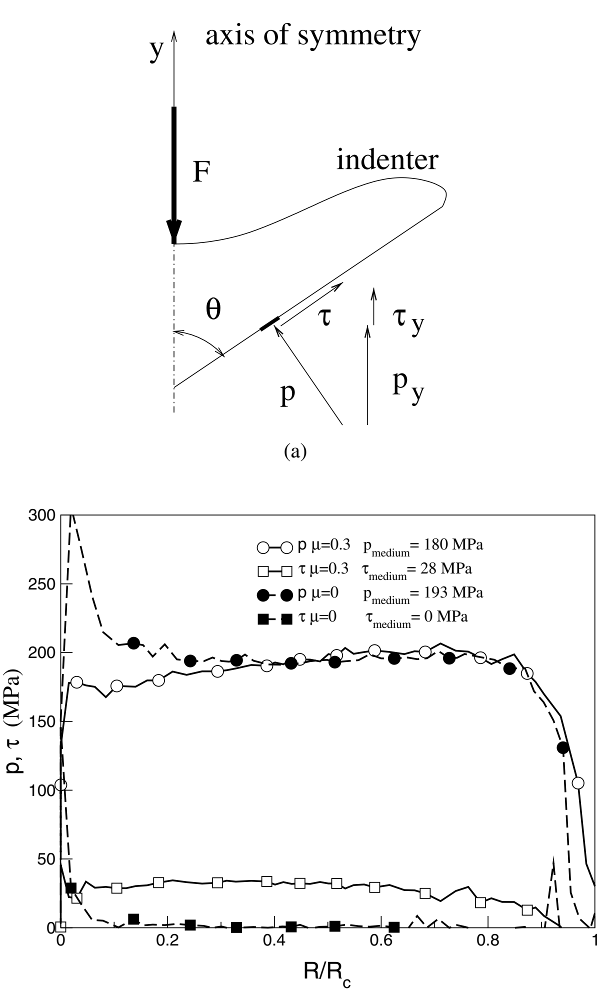

(a)

(b)

Figure 7 Normal pressure and shear stress in indentation. (a) Decomposition of the stresses at the contact. (b) Numerical values for indenter of semi angle 70.3°, for $m = 0.046$, $K = 99$ and $h_g = 1$.

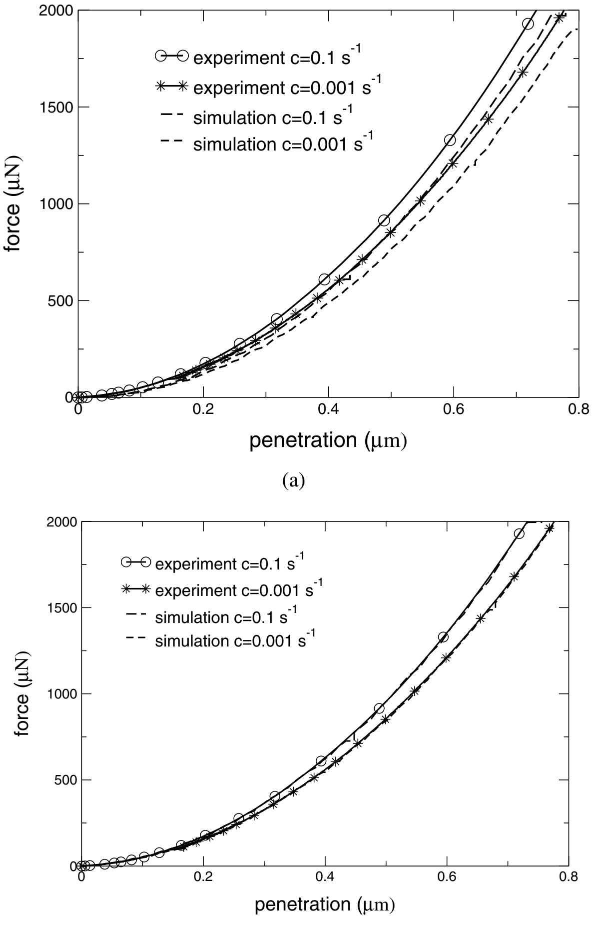

(a)

(b)

Figure 8 Force-penetration curves during loading for a polycarbonate. Comparison between the experimental curves (Berkovich indenter) and the numerical curves ($\mu = 0$, $\theta = 70.3^\circ$ $\rho = 0$ nm and $\rho = 455$ nm). For more legibility the curves for the intermediate loading rate ($c = 0.01$ s^{-1}) are not plotted. (a) $\rho = 0$ nm. (b) $\rho = 455$ nm.

TABLE V Determination of the tip defect and the tip radius of the Berkovich indenter, $\mu = 0$

	A	B	Tip defect h_0 (nm)	Tip radius ρ (nm)
Simulation	59.13	−0.25	0	0
	59.09	0.88	20	322
	59.05	2.08	40	650
Experiment	59.13	1.37		

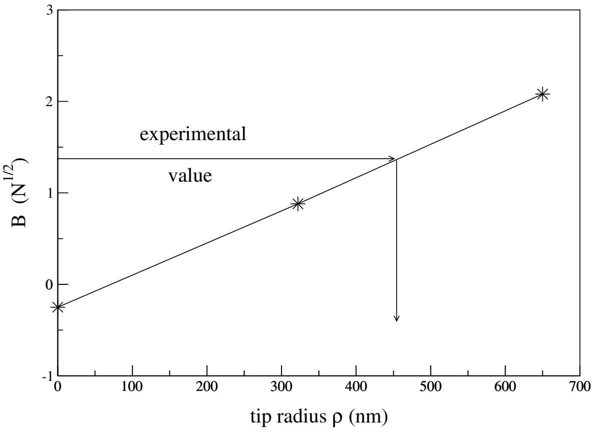

Figure 9 Identification of the indenter tip radius, $\mu = 0$, $c = 0.1$ s^{-1}.

4.3. Identification of the indenter tip defect

The experimental and numerical force-penetration curves are plotted in Fig. 8a, for the frictionless contact. Numerical curves are below the experimental curves, and the difference between them is always similar. In these simulations, it was assumed that the equivalent cone of the Berkovich pyramid had no tip defect. The analytical model in the appendix shows that, a small tip radius has some consequences on the force-penetration curves, even for high penetration depths. This difference can be eliminated with the tip radius ρ (Fig. 8b). We make the assumption that the indenter tip of the Berkovich pyramid may be modeled by a spherical cap. The parameter B of Equation 14 is connected to the semi angle of the indenter, the contact pressure and the indenter tip radius. The semi angle of the indenter is fixed, the contact pressure is already fixed by the rheology. The indenter tip radius is identified in order to have the same parameter B during experiments and simulations. As suggested by the model in the appendix, the slope A does not change significantly with the tip radius (Table V). The tip radius, ρ, and the tip defect, h_0, are equal to 455 nm and 28 nm, respectively for $\mu = 0$ (Fig. 9), and to 580 nm and 36 nm, respectively for $\mu = 0.3$. The difference between the tip radius for the two conditions of friction is quite large but the tip defects are very small compared to the penetration depths (Table IV). Also, it confirms the assumptions that A does not change significantly with the tip radius, and it gives an order of magnitude value of the tip radius.

The difference between the numerical and experimental curves can be also due to the error for the zero-point identification. This is the reason why the tip defect identified may be different from the real one. It is important to note that our work suggests that the difference between numerical and experimental curves is not due to an error on the rheological identification but the real cause is the indenter tip defect or an error on the zero-point identification.

4.4. Identification of the hardening modulus h_g

The indenter of semi apical angle 30° can induce large deformations. The mean value of the equivalent plastic strains computed in simulation is equal to 0.8, and the maximum is about 1.8 (Fig. 5). For these strains, the large strain hardening due to the macromolecules orienting, has already begun (Fig. 3). The hardening modulus, h_g, models the strain hardening of the polymer for high strains. With this indenter, the penetration depths are about 2 μm. The influence of the spherical tip is still large, because the transition depth between the spherical and the conical part is 0.3 μm. We have used the method described in the previous sections to identify the hardening modulus and the indenter tip defect. For penetration depths higher than 1 μm, Equation 14 fits numerical curves (hypothesis $R^{*2} \ll R_c^2$ and $p(\alpha_i) \simeq p(R_i)$ are valid, appendix). The hardening modulus is identified using the force-penetration curves for a loading rate equal to 0.1 s^{-1}. The numerical curves must be superpose or parallel to the experimental curves. If the curves are parallel, the difference is filled by adjusting the tip radius.

Identifications made with penetration depths between 0.75 μm and 1 μm show that the hardening modulus is less than 6 per cent of the value obtained for higher penetration depths ($h > 1$ μm).

This result is very useful for the identification of the viscoplastic parameters of thin films. For a thickness of film of 3 μm, indentation experiments have shown that the penetration depth of this indenter ($\theta = 30°$ and $\rho = 600$ nm) must be lower than 1 μm, in order to have no influence of the substrate.

The apparent hardening modulus decreases as friction increases (Table VI). It is more obvious with this parameter than with the consistency, because the indenter has a power included angle (θ is less) and the friction has more effect on the normal load. The numerical force-penetration curves are not superimposed to the experimental one (Fig. 10a). This difference is adjusted by increasing the indenter tip radius, as presented in the previous section. The values of the tip radius for two conditions of friction are quite close. The tip radius is a little higher than the real one observed with the scanning electron microscope. The force-penetration curves for $c = 0.001$ s^{-1} are not well superimposed (Fig. 10b). The sensitivity to the strain rate identified with the Berkovich indenter depends probably on the strain. This parameter is a little larger for this indenter. This fact is also observed for the curves with $\mu = 0.3$.

TABLE VI Hardening modulus h_g and tip radius of the 30° angle indenter for two values of the Coulomb's friction coefficient

$\mu = 0$	$h_g = 0.8$	$\rho = 660$ nm
$\mu = 0.3$	$h_g = 0.5$	$\rho = 640$ nm

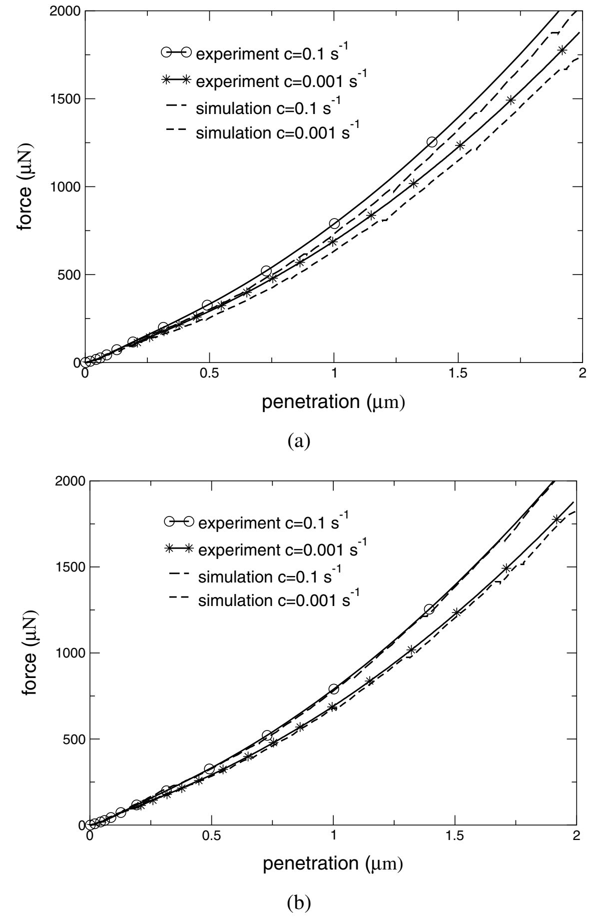

(a)

(b)

Figure 10 Force-penetration curves during loading for a polycarbonate. Comparison between the experimental curves ($\theta = 30°$, $\rho = 600$ nm) and the numerical curves ($\mu = 0$, $h_g = 0.8$, $\theta = 30°$, $\rho = 600$ nm and $\rho = 660$ nm). For more legibility the curves for the intermediate loading rate ($c = 0.01$ s^{-1}) are not plotted. (a) $\rho = 600$ nm. (b) $\rho = 660$ nm.

4.5. Hydrostatic pressure in indentation

In numerical modeling, the plasticity criterion does not include the effect of the hydrostatic pressure, but the code can compute it. The hydrostatic pressure is maximum at the contact interface for the indenter for the 70.3° cone and below the contact for the other one (Fig. 11). In first approximation, the hydrostatic pressure decreases as the radial distance to the indenter tip increases, as in the model of the expansion of a spherical cavity [4]. The values are quite similar for the two indenters. The dark area corresponds to hydrostatic pressure higher than 120 MPa. For such a pressure, the yield stress increases by 40 per cent for a polycarbonate according to Staats-Westover and Vroom [15]. The analytical formula of the hydrostatic pressure in compression is $\frac{\sigma_0}{3}$, and is equal to 30 MPa for small strains. During indentation, hydrostatic pressure is higher than in compression, $\sim\frac{4}{3}\sigma_0$.

5. Discussions

5.1. Analysis of the stress-strain curves

First, the assumption made in Section 3.2 concerning the use of the G'sell Jonas law and more precisely the modeling of large strain hardening of polymers in indentation is valid. While the orientation of macromolecules in tension or compression tests is in the same direction in all the volume, in indentation it occurs more locally, depending of the kind of stress: tension, compression or shear.

The numerical and experimental force-penetration curves are in good agreement. Bisilliat [16] has made tension and compression tests on a polycarbonate. The parameters of the G'sell-Jonas law have been identified from these tests. It is not exactly the same polycarbonate as used there, but it is also possible to compare the stress-strain curves in compression and tension and those obtained in indentation for the two coefficients of friction (Fig. 12).

The rheology in indentation depends on the assumption of the value of the friction coefficient between the indenter and the material. For small strains, the behavior is independent of friction: this behavior has been identified with a Berkovich indenter, where friction has little effects on the force-penetration curves. For higher strains, the stress is lower for $\mu = 0.3$ than for $\mu = 0$, the vertical component of the shear stress τ acting on the indenter $\theta = 30°$ is large enough to increase significantly the normal force. So, it is important to identify previously the coefficient of friction.

For small strains, stresses obtained with the present method are higher than those in tension and close to stresses in compression. Results presented in the previous section have shown that hydrostatic pressure is higher in indentation than in compression. So, we would

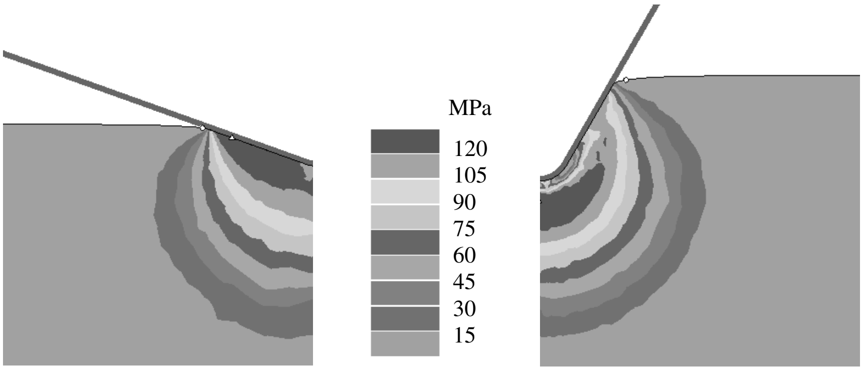

θ = 70.3°   θ = 30° ρ = 600 nm

Figure 11 Hydrostatic pressure in indentation for a polycarbonate for the two indenters.

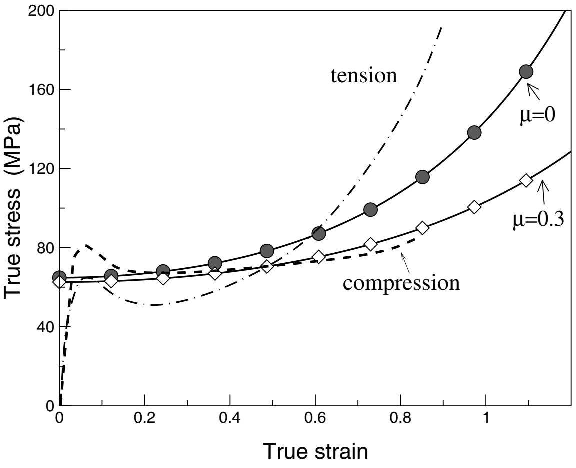

Figure 12 Comparison between the rheology from the present work and those from Bisilliat [16] in compression and tension. Curves are plotted with equation 8 and the parameters in tables 3, 4, and 6, for a strain rate of 10^{-4} s^{-1}.

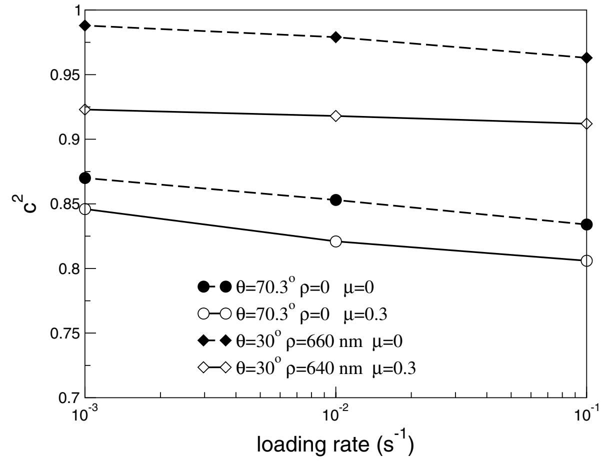

Figure 13 Shape ratio computed with the simulations for two indenters and for three loading rates.

expect that the viscoplastic level in indentation would be higher than the one observed in compression. For high strains, the curves obtained from the present work are between the tension and compression curves. For a coefficient of friction of 0.3, the curve is near the curve obtained in compression. Bisilliat [16] has identified a value of the hardening modulus in compression equal to 0.52. The stress-strain curves for $\mu = 0.3$ are the most representative curves of the rheology of the material, because this coefficient of friction is close to the value deduced from scratch experiments.

The sensitivity to the strain rate obtained with the Berkovich indenter is a little higher than for the other indenter, for which plastic strains are almost five times larger (Fig. 10b). The values of m obtained in indentation are in the same order of magnitude than those in compression and tension and higher than in shear. An increase of two decades of the strain rate implies an increase of 28% in the flow stress, while as the plastic strain increases from zero to one, the associated flow stress reaches a 65% higher value. Although polymers are sensible to the strain rate at room temperature, the effect of deformation in indentation (i.e., the angle of the indenter) is much larger.

5.2. Shape ratio and normal hardness

The shape ratio c^2 is the ratio between the contact depth and the total depth (Fig. 1):

$$c^2 = \frac{h_c}{h} \tag{16}$$

First, consider the shape ratio under load for several loading rates and the two indenters. The shape ratio is always lower than 1, meaning that there is a 'sinking-in' under load (Fig. 13). This ratio is of course independent of the penetration depth for an indenter with a sharp tip. For the 30° indenter the shape ratio increases for small penetrations and becomes constant for penetrations higher than 0.5 μm. The shape ratio decreases as the loading rate increases: the flow stress is greater for the high loading rates, and the elastic part of the deformation is then higher. The factor $\frac{E}{\sigma_0}\tan\beta$ is therefore smaller, the indentation for $c = 0.1\ \mathrm{s}^{-1}$ is more elastic, and the 'sinking-in' is more marked. As expected, the shape ratio decreases as friction at the interface increases. The material cannot go up as much as it was possible without friction, and the 'sinking-in' is increased. As the semi angle of the indenter decreases, deformations become higher and the shape ratio is higher for the indenter of semi angle 30°. The tip defect has negligible influence on the shape ratio for the 70.3° indenter.

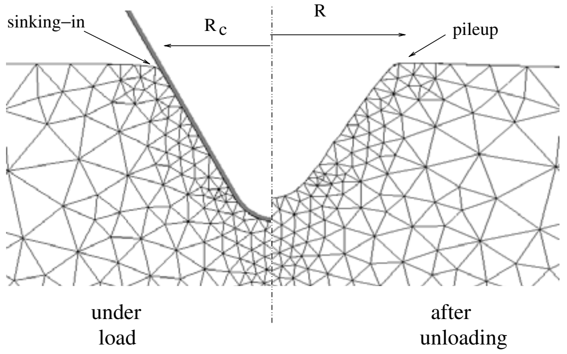

Figure 14 Comparison between the geometry under load and after unloading.

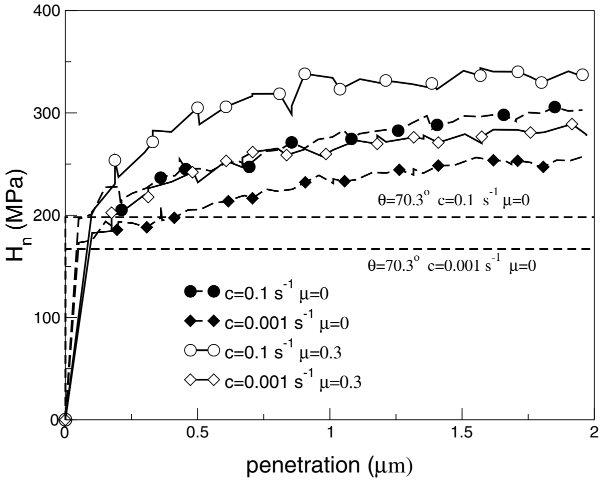

Figure 15 Normal hardness computed with the simulations for two indenters and for two loading rates.

After unloading there is a depth recovery, its value is about 10 percent (Fig. 14). It has been observed for the two indenters in numerical simulation. This elastic recovery is larger for the real sample, according to some observations made with an atomic force microscope. The elastic behavior in simulation is not well modeled, these results only show the first step of the elastic recovery. The next steps are due to the visco-elastic behavior of the polycarbonate. The other important fact is that there is always a pile-up formation after unloading, the value of the shape ratio after unloading is about 1.06. The residual radius, R, is larger than the contact radius, R_c. The residual imprint of the indentation is larger but its depth is smaller. Visco-elastic properties of materials could have opposite effects: the residual radius would become smaller than the contact radius.

For the 70.3° indenter, the normal hardness is independent of the penetration depth (Fig. 15). The tip radius and the coefficient of friction have no important influence on the normal hardness (less than 3%). For small strains, the stress is almost the same for the two conditions of friction at the interface. As the loading rate increases from 0.001 s^{-1} to 0.1 s^{-1}, the hardness increases by 16%: the normal force is higher for $c = 0.1$ s^{-1} and the shape ratio is smaller. For the indenter of semi apical angle 30°, the normal hardness increases as the penetration depth increases and becomes relatively constant for large penetrations. Hardnesses are higher than those computed with the 70.3° indenter, with a maximal increase of 50%. The flow stress is higher for this indenter, because of the strain hardening at large strains. The difference as a function of loading rate is similar to the one observed with the 70.3° indenter. Friction has more of an effect: the hardness increases by 30 MPa for a coefficient of friction equal to 0.3, because the vertical component of the shear stress is added to the vertical component of the normal pressure (Fig. 7a). The normal force is larger and the shape ratio is lower, so the normal hardness increases for $\mu = 0.3$. This friction effect on normal hardness has been observed in indentation on polymers by Briscoe *et al.* [21] and by Ramond-Angélélis [22] in numerical simulation.

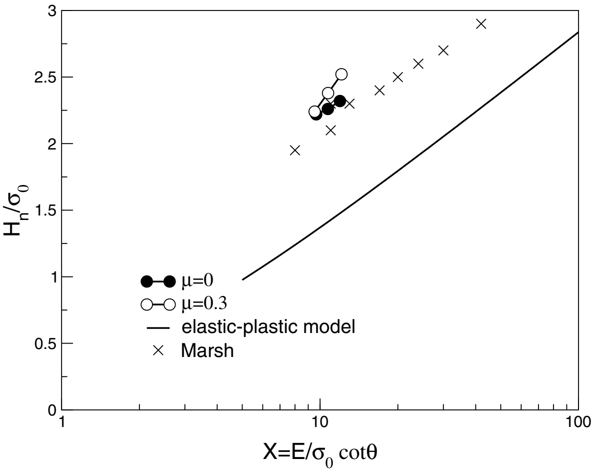

Figure 16 Evolution of the normal hardness over the flow stress ratio as a function of the rheological factor for the indenter of semi apical angle 70.3° and for three loading rates and two conditions of friction.

5.3. Relation between the normal hardness and the flow stress

During simulations of indentation with the indenter of semi apical angle 70.3°, strains are small and the flow stress is relatively constant. Assuming that the strain rate is equal to the loading rate ($\dot{\varepsilon} \sim \frac{\dot{h}}{h}$), the flow stress can be computed and compared to the normal hardness. This comparison is far more complicated and has not been done with the indenter $\theta = 30°$ because the flow stress during loading is not constant and it cannot be well identified. The rheological factor is about 10, and the ratio of the normal hardness to the flow stress is about 2.4 (Fig. 16). The $\frac{H_n}{\sigma_0}$ ratio increases as the rheological factor increases. These values are in a good agreement with those obtained by Marsh [23] with a Vickers pyramid for a diverse range of materials, but they are higher than the elastic-plastic model suggested by Johnson [4] with $\nu = 0.35$.

6. Conclusions

Elastic parameters of polycarbonate has been previously obtained with compression and indentation tests. In this study, the viscoplastic behavior has been modeled with a G'sell-Jonas law. We had to identify three parameters: the sensitivity to the strain rate, the consistency, and the hardening modulus. These parameters have been obtained for 2 values of coefficient of friction by using the nano-indentation test and the numerical modeling of this test.

Stress-strain curves of polycarbonate show a dependence on the friction coefficient, especially at large strains. So, the coefficient of friction has to be determined independently and has to closely represent the real contact conditions. It has been shown that for $\mu = 0.3$, the behavior in indentation is close to the one observed in compression. For this multi-axial test, the strain hardening, observed on polymers in tension or compression, does exist and is close to the value of the strain hardening in compression. Comparisons with compression and tension tests show that our method gives good results. Similar identifications have been also made on a poly(methyl methacrylate) and a thermosetting polymer [19] and show a good agreement with the compression tests. A good agreement with the compression behavior has been found. This method can also be used to identify the rheology of thin polymer films.

Numerical simulation show that the 'sinking-in' effect under load becomes, after unloading, a 'pile-up' effect. The normal hardness is larger for the indenter $\theta = 30^\circ$ and increases as the coefficient of friction and the loading rate increase. For the 70.3° indenter, the normal hardness is about 2.4 times the flow stress.

Acknowledgements

Essilor INTL Coatings Research and Development is acknowledged for its interest for the results and its financial and technical support for part of this work. We wish to express our thanks to Dr P. Montmitonnet for helpful criticisms of this text.

Appendix

It is impossible to make a real indenter with a pointed tip. The tip defect is modeled with a part of a sphere. The static equation along the vertical axis gives the following equation [20] (Fig. 17):

$$F = \underbrace{2\pi \int_0^\alpha \rho d\gamma \rho \sin\gamma p(\gamma) \cos\gamma}_{\text{spherical part}} + \underbrace{2\pi \int_{R^*}^{R_c} r \frac{\mathrm{d}r}{\sin\theta} p(r)\ \sin\theta}_{\text{conical part}} \tag{17}$$

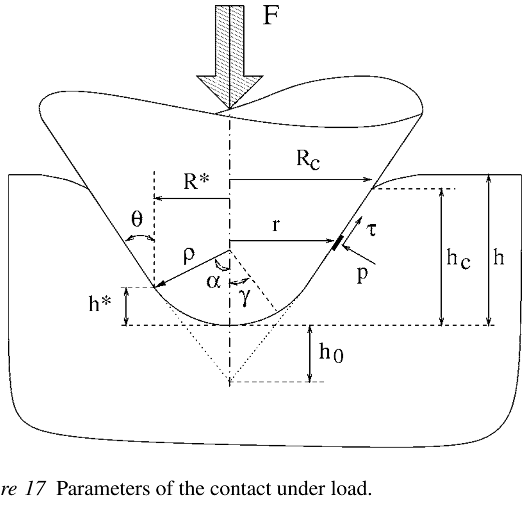

Figure 17 Parameters of the contact under load.

In order to simplify the equation, the friction term is not written. The first part of the integral is related to the normal force acting on the spherical part, while the second one is related to the conical part. The normal pressure is not constant on the interface. The two functions, $\sin\gamma\cos\gamma$ and r do not change their signs on the intervals $[0;\alpha]$, $\alpha < \frac{\pi}{2}$ and $[R^*; R_c]$. The theorem of the mean value is used, where $\alpha_i \in [0;\alpha]$ and $R_i \in [R^*; R_c]$:

$$\begin{aligned} F &= 2\pi\rho^2 p(\alpha_i) \int_0^\alpha \frac{\sin 2\gamma}{2} d\gamma + 2\pi p(R_i) \int_{R^*}^{R_c} r\mathrm{d}r \\ &= \pi\rho^2 p(\alpha_i) \sin^2\alpha + \pi p(R_i)\big(R_c^2 - R^{*2}\big) \\ &= \pi p(\alpha_i) R^{*2} + \pi p(R_i)\big(R_c^2 - R^{*2}\big) \\ &= \underbrace{\pi R^{*2}(p(\alpha_i) - p(R_i))}_{1st\ term} + \underbrace{\pi R_c^2 p(R_i)}_{2nd\ term} \end{aligned}$$

For contact radius R_c higher than the limit radius R^* and assuming that $p(\alpha_i) \approx p(R_i)$, the first term is negligible compared to the second term. The mean pressure $p(R_i)$ is independent of the penetration for $h > h^*$. The contact radius R_c is linked to the shape ratio $c^2 = \frac{h_c}{h}$:

$$R_c = \tan\theta(hc^2 - h^*) + R^* \tag{18}$$

The shape ratio is constant for penetrations higher than the limit penetration h^*. The force has the following expression:

$$F \approx \pi p(R_i)(\tan\theta(c^2 h - h^*) + R^*)^2 \tag{19}$$

The force is related to the square of the penetration. The consistency and the hardening modulus are identified by plotting the square root of the force versus the penetration h:

$$\begin{aligned} \sqrt{F} &\approx Ah + B \\ A &= \sqrt{\pi p(R_i)} \tan\theta c^2 \\ B &= \sqrt{\pi p(R_i)}(R^* - \tan\theta h^*) \end{aligned} \tag{20}$$

The slope A is related to the contact pressure, the shape ratio and the angle of the indenter. B is related to the contact pressure, the θ angle and the geometry of the indenter tip (R^* and h^*). First, the consistency is found ($p(R_i)$ is fixed), and then the tip defect is identified with the parameter B.

References

1. D. TABOR, "The Hardness of Metals" (Clarendon Press, Oxford, 1951).
2. N. R. CHITKARA and M. A. BUTT, *Int. J. Mech. Sci.* **34** (1992) 849.
3. P. LAVAL, PhD thesis, Ecole Nationale Supérieure des Mines de Paris, 1995.
4. K. L. JOHNSON, *J. Mech. Phys. Solids* **18** (1970) 115.
5. W. C. OLIVER and G. M. PHARR, *J. Mater. Res.* **7** (1992) 1564.
6. B. J. BRISCOE and K. S. SEBASTIAN, *Proc. R. Soc. Lond. A* **452** (1996) 439.

7. A. K. BHATTACHARYA and W. D. NIX, *Int. J. Solids Structures* **24** (1988) 881.
8. Y.-T. CHENG and C.-M. CHENG, *J. Mater. Res.* **14** (1999) 3493.
9. T. A. VENKATESH, K. J. VLIET, A. E. GIANNAKOPOULOS and S. SURESH, *Scripta Materialia* **42** (2000) 833.
10. N. TARDIEU, PhD thesis, Ecole Polytechnique, 2000.
11. E. S. BERKOVICH, *Industrial Diamond Review* **11** (1951) 129.
12. S. MATSUOKA, in "Failure of Plastics," edited by W. Brostow and R. D. Corneliussen (Hanser Publishers, Munich, 1986) p. 24.
13. N. BROWN, in "Failure of Plastics," edited by W. Brostow and R. D. Corneliussen (Hanser Publishers, Munich, 1986) p. 98.
14. B. N. LUCAS, W. C. OLIVER, G. M. PHARR and J.-L. LOUBET, in "Stresses and Mechanical Properties," Vol. VI, edited by W.-W. Gerberich, H. Gao, J.-E. Sundgren and S.-P. Baker (Materials Research Society, 1996) p. 233.
15. R. F. STAATS-WESTOVER and W. J. VROOM, *Soc. Plant Engrs.* **25** (1968) 8.
16. M. L. BISILLIAT, PhD thesis, Ecole Nationale Supérieure des Mines de Paris (1997).
17. C. G'SELL and J. J. JONAS, *J. Mater. Sci.* **14** (1979) 583.
18. M. C. BOYCE and E. M. ARRUDA, *Polymer Engineering and Science* **30** (1990) 1288.
19. J.-L. BUCAILLE, PhD thesis, Ecole Nationale Supérieure des Mines de Paris (2001).
20. J. GODDARD and H. WILMAN, *Wear* **5** (1962) 114.
21. B. J. BRISCOE, P. D. EVANS, S. K. BISWAS and S. K. SINHA, *Trib. Int.* **29** (1996) 93.
22. C. RAMOND-ANGÉLÉLIS, PhD thesis, Ecole Nationale Supérieure des Mines de Paris (1998).
23. D. M. MARSH, *Proc. R. Soc.* A **279** (1964) 420.

Received 12 December 2000
and accepted 18 April 2002